

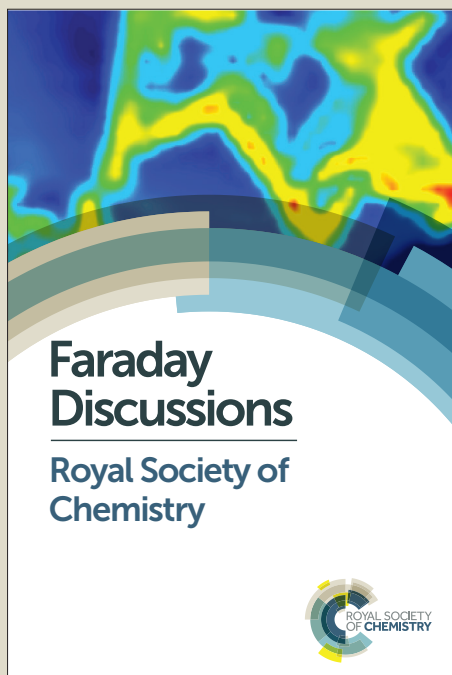
Faraday Discussions

Accepted Manuscript



This manuscript will be presented and discussed at a forthcoming Faraday Discussion meeting. All delegates can contribute to the discussion which will be included in the final volume.

Register now to attend! Full details of all upcoming meetings: <http://rsc.li/fd-upcoming-meetings>



This is an *Accepted Manuscript*, which has been through the Royal Society of Chemistry peer review process and has been accepted for publication.

Accepted Manuscripts are published online shortly after acceptance, before technical editing, formatting and proof reading. Using this free service, authors can make their results available to the community, in citable form, before we publish the edited article. We will replace this *Accepted Manuscript* with the edited and formatted *Advance Article* as soon as it is available.

You can find more information about *Accepted Manuscripts* in the [Information for Authors](#).

Please note that technical editing may introduce minor changes to the text and/or graphics, which may alter content. The journal's standard [Terms & Conditions](#) and the [Ethical guidelines](#) still apply. In no event shall the Royal Society of Chemistry be held responsible for any errors or omissions in this *Accepted Manuscript* or any consequences arising from the use of any information it contains.

Oxygen exchange and transport in dual phase ceramic composite electrodes

John Druce^a, Helena Téllez^a, Tatsumi Ishihara^a and John A. Kilner^{a,b}

a - International Institute for Carbon Neutral Energy Research (wpi-I2CNER), Kyushu University, Nishi-ku, Fukuoka, 819-0395, Japan; Fax: +81(0)92-802-6738; Tel: +81(0)92-802-6738; E-mail: john.druce@i2cner.kyushu-u.ac.jp (JD)

b - Department of Materials, Imperial College London, London, UK, SW7 2BP, Fax: +44(0) 207-594-6745; Tel: +44(0) 207-594-6745;

Abstract

Composites consisting of a perovskite-based electronic or mixed conductor with a fluorite-structured ionic conductor are often used as electrodes in solid oxide electrochemical energy conversion devices. After sintering the materials, there is often evidence for inter-reaction between the two phases, or inter-diffusion of cations or impurities between the two phases. We studied the ¹⁸O exchange properties of a composite consisting of CGO and LSCF in a 50:50 ratio. High resolution ToF-SIMS mapping reveals that ¹⁸O fraction at the very outer surface of grains of the CGO phase is much higher than expected from D^* and k^* values for the single-phase parent material. Surface compositional analysis by ToF-SIMS and Low Energy Ion Scattering (LEIS) spectroscopy suggests the surfaces of the CGO grains in the composite do not show the impurities which typically segregate to the surface in single-phase CGO. Thus the “cleaning” of impurities from the CGO surface by dissolution into the perovskite phase may be one explanation for the apparent enhanced surface exchange for CGO in these composites.

Introduction

Oxygen electrodes for solid oxide electrolyser cells (SOECs) should possess mixed ionic-electronic conductivity (MIEC) under a range of operating conditions. In the case of reversible cells, this entails both oxidising and reducing conditions. Whilst single phase materials such as $\text{La}_{1-x}\text{Sr}_x\text{MnO}_{3+\delta}$ (LSM) and $\text{La}_{1-x}\text{Sr}_x\text{Co}_{1-y}\text{Fe}_y\text{O}_{3-\delta}$ (LSCF) show MIEC behaviour under Solid Oxide Fuel Cell (SOFC) conditions, their ionic conductivities often decrease in the high oxygen activities encountered during SOEC operation due to a drop off in the concentration of charge-carrying oxygen vacancies. This is one of the typical modes of failure of electrodes by delamination¹.

Although single-phase MIEC materials are attractive for electrodes, another way to achieve mixed conduction in both SOEC and SOFC modes is to use macroscopically mixed conducting dual phase ceramic composites. These offer the ability to combine high oxygen diffusivity, normally contributed by an ionically conducting fluorite phase such as $\text{Zr}_{1-x}\text{Y}_x\text{O}_{2-x/2}$ (YSZ) or $\text{Ce}_{1-x}\text{Gd}_x\text{O}_{2-x/2}$ (CGO),

with electronic conduction, typically from a perovskite-structured phase such as LSM or LSCF. In this case, the ionic conductivity is dominated by the fluorite phase and expected to be high in both SOFC and SOEC modes (i.e. the oxidising conditions experienced as anodes under electrolysis mode as well as reducing conditions for cathodes under SOFC mode).

However, the high temperatures required to sinter the materials can lead to inter-reaction. In the case of LSM with YSZ, this can result in the formation of secondary phases such as $\text{La}_2\text{Zr}_2\text{O}_7$ which block oxygen transport)^{2,3}. Although CGO and LSCF are not believed to react to form secondary phases^{4,5}, there is evidence that cation inter-diffusion does occur between the two phases⁶⁻⁹. Particular attention has been paid to diffusion of both transition metals and the larger La and Sr cations from the perovskite into the CGO⁷, although the solubility of Ce and Gd in the perovskite is likely to be low^{10,11}. However, the effect of such inter-reaction on the overall materials properties, such as oxygen surface exchange, are not yet known. It has even been proposed that the diffusion of transition metal cations into the fluorite phase could enhance its electro-catalytic activity towards oxygen incorporation^{12,13}.

The combination of ^{18}O isotopic labelling experiments with Secondary Ion Mass Spectrometry (SIMS) is an attractive combination to study the mechanisms of oxygen exchange. Methods such as electrochemical impedance studies and electrical conductivity relaxation provide information averaged over an entire macroscopic sample, and as such it is difficult to extract any microstructurally-resolved information on the role of the two phases. On the other hand, SIMS instruments can provide a probe on the order of 100 nm, allowing localised information to be extracted, highlighting the active sites for oxygen incorporation^{14,15}.

Although previous reports of IEDP-SIMS studies on composites used quadrupole SIMS instruments^{12,16}, this type of SIMS suffers from the drawback that mass detection is sequential. That is, the masses to be studied must be chosen beforehand, and only a single signal can be monitored at one time. Therefore, it is impossible to obtain, say, both the ^{16}O and ^{18}O intensities from the same point – one must be recorded first, which entails the removal of some material (of the order of 50 nm in depth) by sputtering. The second channel is then recorded by rastering the ion beam a second time across the area of interest. The information in the second scan hence comes from a slightly deeper depth. Therefore, obtaining information about the distribution of cations as well as the oxygen isotopes would consume a large depth of the sample. On the other hand, in contrast to quadrupole SIMS, Time of Flight (ToF-SIMS) offers parallel ion detection, hence the entire mass

spectrum is recorded for every pixel of the image at each depth^{17,18}. Therefore, it is possible to extract far more information about the distribution of chemical and isotopic composition in the sample by the use of ToF-SIMS. In this work, we exploit this combination of isotope exchange and surface analysis by two complementary ion beam techniques, namely Time of Flight (ToF)-SIMS and Low Energy Ion Scattering spectroscopy (LEIS), to study oxygen exchange in these materials. The former technique offers high chemical sensitivity and lateral resolution, whilst the latter quantitatively probes the elemental composition of the very outer atomic surface of a material¹⁹⁻²¹.

Experimental

Commercially available powders of $\text{Ce}_{0.9}\text{Gd}_{0.1}\text{O}_{1.95}$ (CGO, Nextech, USA) and $\text{La}_{0.6}\text{Sr}_{0.4}\text{Co}_{0.2}\text{Fe}_{0.8}\text{O}_{3-\delta}$ (LSCF, Praxair, USA) were mixed in a 50:50 (by weight) ratio by ball milling overnight (longer than 12 hours) in ethanol. After drying the powder blends, they were pressed into pellets and sintered at 1250 °C for 4 hours.

The sintered pellets, with density (as estimated by the Archimedes method) greater than 95% of theoretical, were ground flat with SiC and then polished with diamond suspension. One set of these samples was analysed in the “as-polished” state (see below for experimental details of the characterisation techniques), whilst the other samples were used for the ^{18}O exchange experiments^{19,22}. This methodology involves a pre-anneal in research grade oxygen (of nominally natural isotopic abundance) for at least 10 times the duration of the subsequent exchange anneal, before the introduction of 200 mbar of oxygen gas enriched in ^{18}O and the (shorter) exchange anneal. The ^{18}O diffusion profiles were then measured by ToF-SIMS, and the surface composition of the samples analysed by Low Energy Ion Scattering (LEIS) spectroscopy.

The duration of the isotope exchanges (900 s at 500 °C and 1200 s at 700 °C) were chosen based on data in the literature for the two constituent phases^{23,24}. Key parameters for the exchange are summarised in table 1. The diffusivity of LSCF is lower than that of CGO by one to two orders of magnitude lower at the temperatures of interest. Therefore, the normalized surface isotopic fractions will essentially be governed by the surface exchange coefficient, k^* . Note that under the exchange conditions chosen, the isotopic fraction in the CGO is expected to be virtually zero, whilst that in the LSCF should be 30 – 40 %. In other words, we expect significant contrast in the ^{18}O isotopic fractions between the two phases.

Table 1 Oxygen-18 exchange conditions used in this work

Temp.	Phase	D* (cm ² s ⁻¹)	k* (cms ⁻¹)	Anneal Time (s)	Ld (μm)	h'	C's [Cs] (%)	Reference
500 °C	CGO	5 x 10 ⁻¹⁰	2 x 10 ⁻⁹	1058	14.5	0.0029	0.33 [0.51]	²⁴
	LSCF	6 x 10 ⁻¹²	3 x 10 ⁻⁸		1.6	0.3984	32.8 [31.3]	²³
700 °C	CGO	2 x 10 ⁻⁸	4 x 10 ⁻⁸	1590	112.8	0.0113	1.3 [1.4]	²⁴
	LSCF	3 x 10 ⁻⁹	1 x 10 ⁻⁶		43.7	0.7280	48.4 [46.2]	²³

Measurement of oxygen isotope distributions

Time-of-Flight Secondary Ion Mass Spectrometry (ToF-SIMS V, Ion-ToF GmbH., Germany) was used to analyse the lateral distribution of various elements of interest (e.g. cations characteristic of the two phases) at the sample surface, as well as the distribution of the ¹⁸O isotopic tracer, as it provides isotopically-resolved information of the elemental composition. The depth profiles were performed in dual beam mode, with sputtering by a 2 keV Ar⁺ beam interlaced with the analysis cycles. After profiling, the sputter rates were calibrated by measuring the final crater depth by 3D microscopy (LEXT OLS 4000, Olympus, Japan). To avoid inaccuracies in the determination of the oxygen isotope fractions due to detector saturation, Selective Attenuation of Secondary Ions (SASI)²⁵ was applied to the ¹⁶O⁻ and ¹⁸O⁻ signals, with the attenuation level determined by the instrument software for each species, adjusted automatically throughout the profile.

After depth calibration, the intensities for the ¹⁶O⁻ and ¹⁸O⁻ were extracted from the data, and values for the kinetic parameters D* and k* (oxygen diffusion and surface exchange coefficients, respectively) were determined by fitting Crank's solution to the diffusion equation for a semi-infinite medium including surface exchange limitation (equation 1²⁶) in MATLAB (The Mathworks, USA). In this equation, $C_{(x)} = \frac{I(^{18}\text{O}^-)}{I(^{16}\text{O}^-) - I(^{18}\text{O}^-)}$, calculated from the secondary ion intensities $I(^{16}\text{O}^-)$ and $I(^{18}\text{O}^-)$, is the observed isotope fraction at depth x, C_{bg} is the fraction of the ¹⁸O isotope in the solid immediately prior to the exchange (taken as the natural isotopic abundance of ¹⁸O), C_g is the fraction of the ¹⁸O tracer in the gas phase (95 %), and t is the duration of the isotope exchange anneal.

Equation 1

$$C'_{(x)} = \frac{C_{(x)} - C_{bg}}{C_g - C_{bg}} = \operatorname{erfc}\left(\frac{x}{2\sqrt{D^*t}}\right) - \exp\left(x\frac{k}{D^*} + \frac{k^2t}{D^*}\right) \operatorname{erfc}\left(\frac{x}{2\sqrt{D^*t}} + \sqrt{\frac{k^2t}{D^*}}\right)$$

For the analysis of the lateral distribution of the ^{18}O tracer at the sample surfaces, ToF-SIMS imaging analysis was conducted with the instrument operated in the “fast imaging” mode, offering high lateral resolution (approximately 100 nm spot size), and unit mass resolution. Rather than bursting the beam to reduce the primary ion current, and hence the secondary ion currents²⁷, saturation of the detector by the intense oxygen secondary ion currents was again avoided by attenuation of the signals at m/z 16 u (attributed to $^{16}\text{O}^-$) and 18 u (attributed to $^{18}\text{O}^-$) by SASI²⁵. For the imaging analysis, the attenuation factors were fixed as “high” (attenuation by a factor of 87) for m/z 16 u and “low” (attenuation by a factor of 7.8) for m/z 18 u.

Surface Analysis by Low Energy Ion Scattering (LEIS) Spectroscopy

Low Energy Ion Scattering (LEIS) spectroscopy measurements of the composition of the very outer monoatomic layer of the samples were performed using a Qtac¹⁰⁰ instrument (Ion-ToF GmbH., Germany). Primary ion beams of $^4\text{He}^+$ (accelerated to 3 keV) and $^{20}\text{Ne}^+$ (accelerated to 6 keV) were directed to the sample surface at normal incidence, and the energy distribution of ions backscattered through 145° was measured by a double toroidal electrostatic analyser. Further details of the LEIS technique in general are given in references^{28,29}, and more details on the specific experimental setup are given in reference³⁰. Prior to analysis, adventitious atmospheric contamination (*e.g.* adsorbed moisture and hydrocarbons), which would otherwise obscure information on the composition of the very outer monolayer, was cleaned from the sample surfaces by exposure to reactive atomic oxygen³¹.

Results

Microstructure and Assignment of Phases

Figure 1 shows ToF-SIMS negative ion maps representing the microstructure of the composites. The image on the left shows the intensity at m/z 88 u. Although the mass of the most abundant isotope of Sr is 87.91 u (85.58% abundance), the signal at m/z 88 u is most likely due to $^{56}\text{Fe}^{16}\text{O}_2^-$ fragment ions rather than negatively charged $^{88}\text{Sr}^-$ ions. However, since both Sr and Fe arise from the LSCF phase, the resolution of this possible interference is not necessary for the purposes of distinguishing between the two phases in this image, and the map at m/z 88 u is deemed characteristic of the LSCF.

On the other hand, the signal at m/z 188 u is attributed predominantly to GdO_2^- , and so taken as characteristic of the CGO phase. The two negative secondary ion maps presented are clearly the inverse of one another, and the overlay of the two signals shows that the distribution of these two elements is complementary, as expected for the two phases.

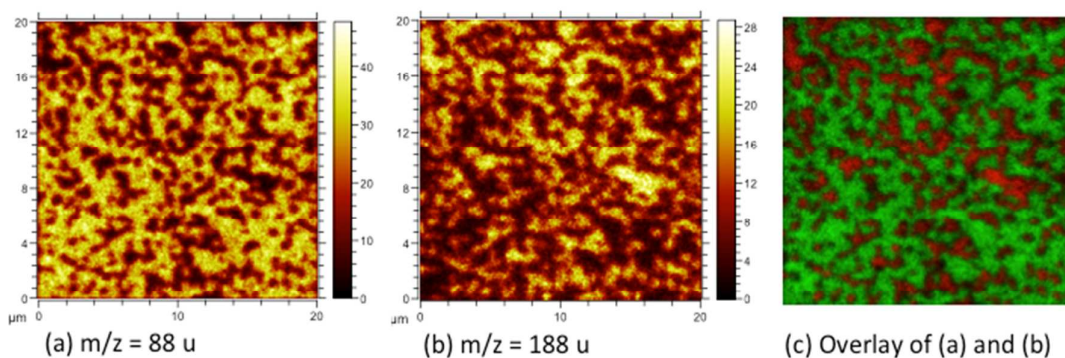


Figure 1 ToF-SIMS negative secondary ions images for (a) m/z 88 u (FeO_2^-) and (b) m/z 188 u (GdO_2^-) and two-channel overlay of the two in green and red respectively

The grain sizes of the two phases measured from SEM images were 620 nm for the LSCF and 750 nm for the CGO. In comparison, the grain sizes in the single phase CGO and LSCF samples, sintered under the same conditions, were around 2 μm and 300 nm respectively. Grain growth of the LSCF grains during sintering of the composite appear to be suppressed by the presence of neighbouring grains of CGO. On the other hand, the size of the CGO grains in the composite sample are more than twice that in the single phase parent material. Cobalt is often added to CGO as a sintering aid^{32,33}, and it is possible that Co diffusing from the LSCF may act in a similar way.

^{18}O Isotope Exchange Experiments

“Macroscopic” Isotope Diffusion Profiles at 500 °C

Isotope exchange profiles in the pure LSCF and the CGO-LSCF composite exchanged at 500 °C and obtained by dual beam ToF-SIMS sputter depth profiling are shown in Figure 2. The fit of the solution to the diffusion equation (Equation 1) to the experimentally determined profile for the LSCF agrees reasonably well, and returns values of $9.3 \times 10^{-12} \text{ cm}^2\text{s}^{-1}$ and $3.0 \times 10^{-8} \text{ cm s}^{-1}$ for the diffusivity, D^* , and surface exchange, k^* , coefficients respectively, which are very close to those previously obtained²³. As is clear from the inset, at greater depths, the experimental profile deviates from the analytical solution. This is probably indicative of a fast grain boundary diffusion pathway, which may begin to dominate at lower temperatures. Such a change from bulk-dominated to grain boundary dominated transport has previously been observed for mixed conducting perovskites²³.

Unfortunately, the sputter depth profile was terminated before reaching the region $6 \leq \left(\eta = x / \sqrt{D_b^* t} \right) \leq 10$, which is necessary for the accurate determination of grain boundary diffusion product^{25, 34, 35}. Therefore, the contribution of the grain boundary was neglected; this does not seem to have affected the fit of the analytical solution adversely.

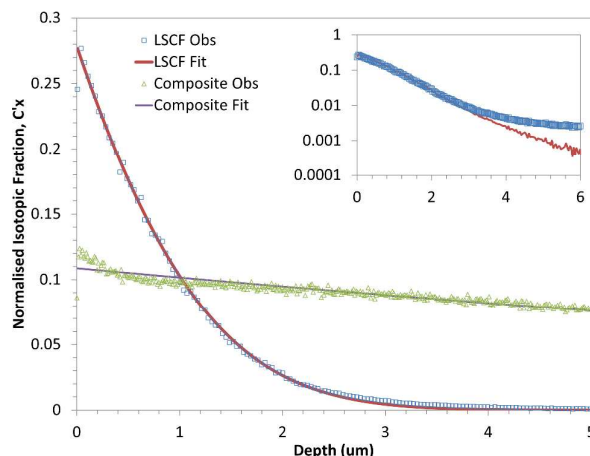


Figure 2 Oxygen-18 diffusion profiles and associated fits for pure LSCF and a 50:50 CGO-LSCF composite subjected to isotope exchange at 500 °C. Inset shows data for LSCF plotted on a logarithmic scale to highlight deviation at greater depths.

Figure 2 also shows the isotope diffusion profile for the composite exchanged at 500 C. The diffusion length here is clearly far longer than the LSCF, and the fit of Equation 1 to the profile yields “effective” values of $D^* = 1.6 \times 10^{-9} \text{ cm}^2\text{s}^{-1}$ and $k^* = 1.3 \times 10^{-7} \text{ cms}^{-1}$. Note that we term these values “effective” parameters as analysis using Equation 1 implies one-dimensional diffusion in a homogeneous medium, rather than the more realistic situation of three dimensional diffusion between two phases which occurs in the composite. This type of analysis has previously been applied successfully to composites including those in the CGO-LSCF^{16, 36} and YSZ-LSM¹³ systems. The D^* value is around three times higher than the literature value for CGO²⁴. Although it was not possible in the present work to measure the diffusion profile in CGO at this temperature, due to the low k^* value, measurements on samples prepared from this CGO powder as part of another study showed diffusivities around 5 times higher than reported in²⁴, possibly due to its relatively low impurity content³⁷. Thus the diffusivity of the composite is comparable to that of the single phase CGO. On the other hand, the k^* value obtained for the present composite is four times higher than previous reported and measured in this work for single phase LSCF, showing some enhancement in the effective surface exchange rate in this composite.

This type of analysis has previously been applied to fit diffusion profiles and extract “effective” D^* and k^* values for composites^{13, 16, 36}, and the fit of equation 1 to the present data agrees well deeper into the sample. However, a feature is evident in the profile for the composite at shallow depths, showing an increased isotopic fraction not described by the analytical solution of Equation 1. The artefact is not seen in the diffusion profile for the single-phase LSCF (also in Figure 2), and is likely to be related to the mechanism of oxygen exchange in the composite. Since the length of the feature is comparable to the diffusion length in LSCF, it may indicate that oxygen is incorporated into the LSCF and diffuses a short distance before being transferred to the CGO. Although this feature was not reported in the previous work, this may be because they were performing linescan analyses of cross sections³⁸, and the lateral resolution in these measurements (around 10 μm) is insufficient to resolve features on this length scale.

¹⁸O Isotopic Fraction mapping at low temperatures (500 °C)

Figure 3 shows results of the ToF-SIMS isotopic mapping of the composite exchanged at 500 °C. Parts (a) and (b) are the secondary ion maps for the $^{16}\text{O}^-$ and $^{18}\text{O}^-$ oxygen isotopes respectively. Part (c) shows the intensity map of the signal at m/z 88 u (as discussed above, this is attributed to FeO_2^- ions, taken to be characteristic of the LSCF phase). Although some contrast between the two phases is evident in the oxygen images – *i.e.* the CGO regions are brighter - this appears in both the $^{16}\text{O}^-$ and $^{18}\text{O}^-$ maps and is therefore probably related to differences in the secondary ion yields of oxygen between the two phases³⁹, and not the exchange properties. On the other hand, we can account for this by calculating the ^{18}O isotopic fraction on a pixel-by-pixel basis ($C_{x,y} = \frac{^{18}\text{O}_{x,y}}{^{16}\text{O}_{x,y} + ^{18}\text{O}_{x,y}}$), which normalises out the effect of different secondary ion yields for the two phases. The resulting image is shown as Figure 3 (d). Note that the values shown in this figure have not been normalised to the isotopic fraction in the exchange gas or to the natural isotopic abundance of ^{18}O . However, since the former is rather high (95 at.% ^{18}O), and the latter low (0.204 % ^{18}O), this normalisation would not qualitatively affect the image.

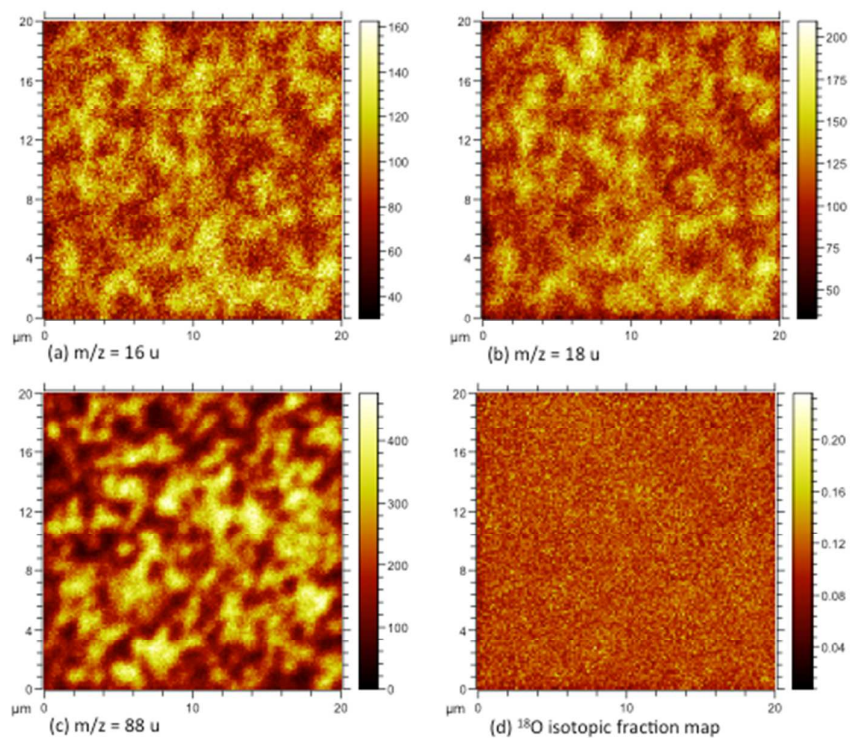


Figure 3 ToF-SIMS negative secondary ion images of a 50:50 CGO-LSCF composite exchanged at 500°C. (a) m/z 16 u (^{16}O), (b) m/z 18 u (^{18}O), (c) m/z 88 u (FeO_2^- , Indicative of LSCF phase), (d) oxygen isotopic fraction map.

Considering the rather large difference in the expected isotopic fractions for the two phases under the present annealing conditions (0.005 for CGO and 0.313 for LSCF, from table 1), relatively little contrast is evident in Figure 3(d). Close scrutiny of the image suggests some marginally brighter patches corresponding to grains of LSCF indicated in Figure 3(c), although this is not as significant as might be expected from the literature values.

The surface ^{18}O isotopic fraction may also be determined for each phase by extracting data from regions of interest corresponding to the two phases. This was performed in the SurfaceLab “Measurement Explorer” Software, provided by IonToF GmbH., Germany. This procedure gives average isotopic fraction values of 0.099 for the CGO and 0.101 for the LSCF regions. The ^{18}O surface isotopic fraction for the CGO is around 20 times higher than that expected for the single-phase material under the same exchange conditions, whilst that for the LSCF is about a third of that expected for the LSCF, and indeed seen in Figure 2 for the LSCF sample exchanged at the same time.

From the extracted surface isotopic fractions, we can calculate “apparent” surface isotopic fractions, assuming that the two constituent phases behave as isolated phases in the exchange. From this point of view, we obtain values of $k^* = 6.8 \times 10^{-8} \text{ cm s}^{-1}$ for the CGO (around 30 times the

value of $2 \times 10^{-9} \text{ cms}^{-1}$ reported by Manning *et al.* ²⁴) and $9.5 \times 10^{-9} \text{ cms}^{-1}$ for the LSCF (a third of the value of $3 \times 10^{-8} \text{ cms}^{-1}$ determined for the LSCF sample exchanged at the same time).

¹⁸O Isotopic Fraction mapping at high temperatures (700 °C)

A similar ¹⁸O isotopic fraction mapping experiment is shown in Figure 4 for the sample exchanged at 700 °C. Again, the two phases are clearly resolved in the SIMS maps for both ¹⁶O and ¹⁸O isotopes (Figure 4(a) and (b)), and for the signal at m/z 88 u, characteristic of the LSCF phase (Figure 4(c)). As discussed for the previous case, we must calculate the oxygen isotopic fraction on a pixel-by-pixel basis to account for differences in useful ion yield between the two phases, as shown in Figure 4(d). Two things are evident from this latter image; firstly, a better microstructural contrast than seen in Figure 3(d) is achieved. Secondly, the contrast is the inverse of what is expected from the properties of the parent materials – the isotopic fraction in the CGO phase should be around 0.014, whilst that in the LSCF should be much higher, around 0.462 (table 1). However, the ratios in Figure 4(d) show far less contrast than expected, and surprisingly, the CGO is brighter in the ¹⁸O tracer.

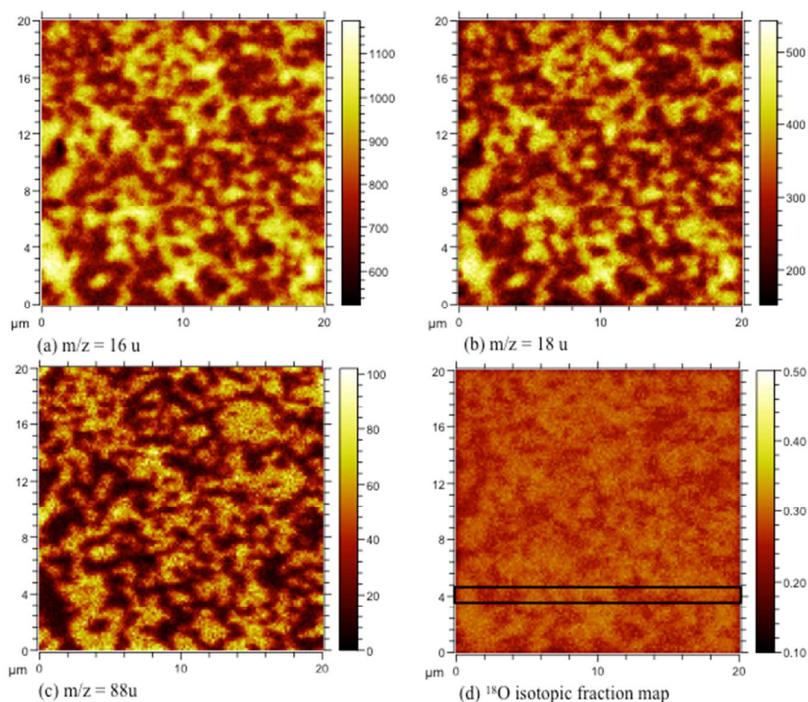


Figure 4 ToF-SIMS negative secondary ion images of CGO-LSCF composite exchanged at 700 °C. (a) m/z 16 u (¹⁶O) image, (b) m/z 18 u (¹⁸O) image, (c) m/z 88 u (LSCF: FeO_2^- image, (d) oxygen isotopic fraction map. The box in (d) indicates the region from which the line scans shown in Figure 5 were extracted.

As discussed in several recent publications ^{25, 27, 40}, if the typically more intense ¹⁶O signal saturates the SIMS detector, the ¹⁸O isotopic fractions will be overestimated. Since the CGO phase shows a higher ion yield for oxygen, there is a danger that this may induce

some detector saturation and an overestimate of the ^{18}O isotopic fraction for the CGO phase. Care has been taken to exclude the possibility of saturation, by the use of SASI⁴¹ during data acquisition, and by cross checking that the same distribution is obtained calculating the isotopic fraction from the (unsaturated) peaks at $m/z = 32$ u ($^{16}\text{O}^{16}\text{O}$), 34 u ($^{16}\text{O}^{18}\text{O}$) and 36 u ($^{18}\text{O}^{18}\text{O}$). Therefore the isotope fraction map in Figure 4(d) does indeed reflect the true distribution in the composite.

Figure 4(d) indicates a region from which the linescans shown in Figure 5 were extracted. The top plot shows the intensity profile across Figure 4(c), indicating the intensity of the signal characteristic of the LSCF phase (m/z 88 u, attributed to Fe_2O). The bottom plot shows the profile in the ^{18}O isotopic fraction (C'_x) Figure 4(d) in the same region. The variation in the oxygen isotope fractions is not as large as the variation of the signal at m/z 88 u, because ^{18}O has been incorporated in both phases. Despite this, the anti-correlation between the intensity of the m/z 88 u signal (i.e. the LSCF) and the ^{18}O isotopic fraction is clear from these two plots; valleys in the plot of the oxygen isotope fraction match peaks in the plot of the signal at m/z 88 u, and vice versa. Hence it becomes clear from this analysis that the isotopic fraction in grains of the CGO phase is in fact surprisingly higher than that in the LSCF. Since the diffusivity of CGO is still higher than that of LSCF at this temperature, the value of k^* , the surface exchange coefficient, controls the surface isotopic fraction. Therefore, the higher ^{18}O isotopic fraction for the CGO grains implies that k^* is higher for the CGO grains in the composite than for the LSCF grains.

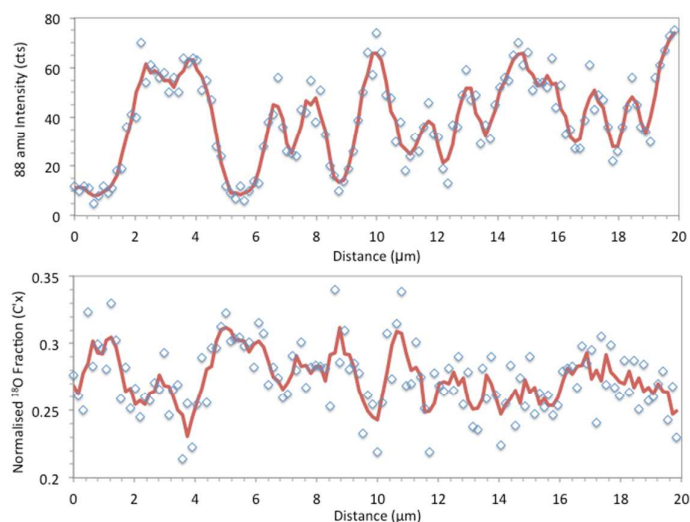


Figure 5 Linescans extracted from region indicated in isotopic mapping data of Figure 4. The points show the data, whilst the lines have been smoothed by a 3-point moving average as a guide to the eye.

To obtain a more precise representative value of the surface isotopic fractions in each phase, the same procedure as for the sample exchanged at 500 °C was followed, by extracting from the data only those regions corresponding to CGO or LSCF respectively, and taking the intensities of $^{16}\text{O}^-$ and $^{18}\text{O}^-$ in those subsets of the data. This gives values of the surface isotopic fraction of 0.291 for the CGO and 0.267 for the LSCF. These values are averaged over all the grains corresponding to each phase (*i.e.* not the maximum values), and agree well with the linescans plotted in Figure 5. Using these surface isotopic fractions along with literature values of D^* for the two phases^{23,24} to estimate their apparent surface exchange coefficients gives values of $4.2 \times 10^{-7} \text{ cm s}^{-1}$ for the LSCF (about 0.42 of the $1 \times 10^{-6} \text{ cm s}^{-1}$ reported for single phase LSCF²³), and $k^* = 1.2 \times 10^{-6} \text{ cm s}^{-1}$ for the CGO, which is a factor of 30 times higher than the value of $4 \times 10^{-8} \text{ cm s}^{-1}$ reported for the single phase parent material²⁴, and indeed even around 3 times higher than the apparent value for the LSCF phase in this composite.

Surface Analysis of Composites and Pure End Members

Before discussing possible reasons for this apparent enhancement, we must also consider the surface composition of the composites. It is known that cation interdiffusion can occur between the two phases at sintering and operation temperatures⁷⁻⁹, and this may explain some of the observed changes in surface exchange behaviour.

Low Energy Ion Scattering (LEIS) Spectroscopy

The $^4\text{He}^+$ (@3 keV) LEIS spectrum for the polished CGO pellet Figure 6(a) shows two peaks, one for oxygen ($\sim 1150 \text{ eV}$), and a second at higher energies representing both Ce and Gd ($\sim 2750 \text{ eV}$), which are too close in mass to be resolved under the present scattering conditions. A small amount of Si is also evident as a surface contaminant. On annealing (Figure 6(b)), the coverage of the rare earth elements decreases, whilst several contamination peaks (Na, Si and K or Ca) appear. These are believed to be impurities segregating from the bulk, which is consistent with previous reports both on CGO⁴² and on the closely related fluorite yttria stabilised zirconia⁴³.

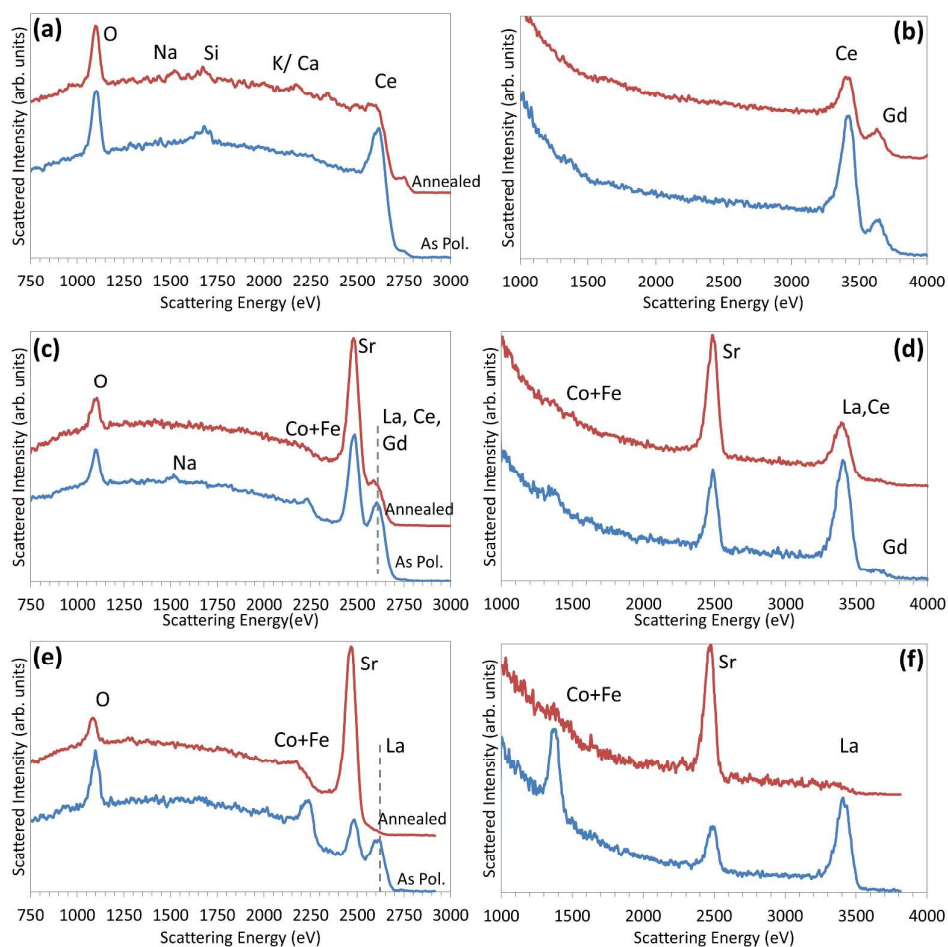


Figure 6 LEIS analysis of samples as-polished and after annealing at 700 °C for (a,b) CGO, (c,d) 50:50 composite and (e,f) LSCF. Spectra taken using $^4\text{He}^+$ at 3 keV (a,c,e) and $^{20}\text{Ne}^+$ at 6 keV (b,d,f).

The evolution of the surface composition of the LSCF, shown in Figure 6(e,f), is similar to that already reported in ref. ⁴⁴. The as-polished spectra show peaks for all elements expected at the surface, although the Fe and Co components are not resolved under the present scattering conditions. Following annealing, Sr segregates towards the surface, at the expense of the coverage of the transition metals and lanthanum, which are virtually undetectable at the surface after annealing at 700 °C, and the outer layer is comprised of Sr and O, as generally observed in most commonly used solid oxide electrode materials ⁴¹.

Figure 6(c,d) shows LEIS spectra for pellets of the composite as-polished and after annealing at 700 °C. Whilst spectra for the unfired powder blend (not show) were a linear combination of the spectra for the parent CGO and LSCF powders, the spectra for the polished composite (Figure 6(c,d), respectively) show a more intense Sr peak than expected from a combination of the spectra for the polished single-phase parent materials. The excess signal in the polished composite may be due to Sr

at the surface of the CGO grains which has diffused into the CGO upon sintering. This is in interesting contrast to a previous SIMS study on CGO-LSCF diffusion couples, which suggested that La was more prone to diffuse into CGO⁸. Finally, we note that Figure 6(c) shows a small amount of sodium contamination for the as-polished composite.

On annealing, the spectra for the annealed CGO-LSCF composites show a further increase in the Sr coverage at the surface, indicating that the LSCF phase in the composite undergoes a similar dominant Sr segregation to the single-phase material. The intensity of the Sr peak is greater for the composite than for the LSCF single-phase material, imply that the extent of segregation is either greater in the composite. This could be because segregating Sr may also migrate across the surface to neighbouring grains of CGO. We note that the images at m/z 88 u shown in Figure 1, Figure 3 and Figure 4 above were obtained in negative polarity, and as such are probably due not to $^{88}\text{Sr}^-$ (Sr as an electropositive element is unlikely to form negative secondary ions), but to FeO_2^- . In fact, the image at m/z 104 u (SrO^-) did not show such clear contrast, which may support this interpretation of migration of segregated Sr to the CGO.

In Figure 6(c) A peak is also evident at a slightly higher energy (around 2750 eV) for the annealed composite, corresponding to either La (*i.e.* from the LSCF) or Ce (from the CGO) – the two cannot be resolved under the present conditions. The latter would suggest the surfaces of the CGO grains in the composite are cleaner than those in the single-phase parent CGO material.

This is also consistent with the absence of the impurities such as Na, Si, Ca which are seen for the CGO pellet, but not the composite. Figure 7 is an enlarged version of the energy range corresponding to Na, Si and Ca impurities for the CGO and composite pellets, both before (*i.e.* as polished) and after annealing. The as-polished CGO already shows a small Si impurity, which increases upon annealing, with the appearance of peaks for Na and Ca. These contaminants are typical for fluorite electrolyte materials after annealing^{42, 43, 45}. In contrast, although the as-polished pellet of the composite did show a small Na contamination peak, none of the impurity peaks (Na, Si, Ca) seen for the single phase CGO are evident after annealing. This also suggests that the surfaces of the CGO in the composites are indeed cleaner. It is possible that grains of the neighbouring perovskite phase may incorporate these impurities in solid solution, effectively “soaking up” the impurities which tend to segregate to the surface of the fluorite grains and block surface exchange.

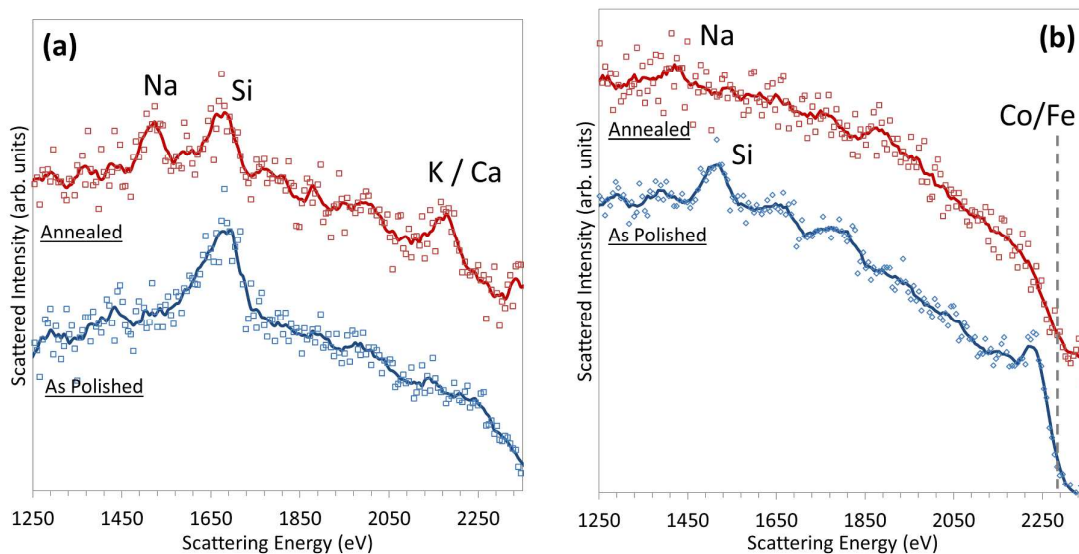


Figure 7 LEIS spectra ($^4\text{He}^+$ @ 3 keV) of light contaminants on (a) CGO and (b) CGO-LSCF composite as-polished and after annealing at 700 °C, and detail showing effect of annealing on composite and CGO surface.

The transition metals might also be expected to play a significant role in the surface exchange properties. However, these are barely detected at the surface of the composites (Figure 6(d)), and seem to be in proportion to their concentration in the single-phase material. This suggests that the signal arising only from transition metal cations in the outer surface of the LSCF grains, which disappear with increasing annealing temperature. Secondary ion maps of signals characteristic of the two transition metals, Co and Fe (Figure 8), show strong contrast between the LSCF and CGO phases, with virtually no signal detected in the CGO grains. The edges of the grains are sharp, implying there has been no significant diffusion of transition metals from the LSCF to the CGO .

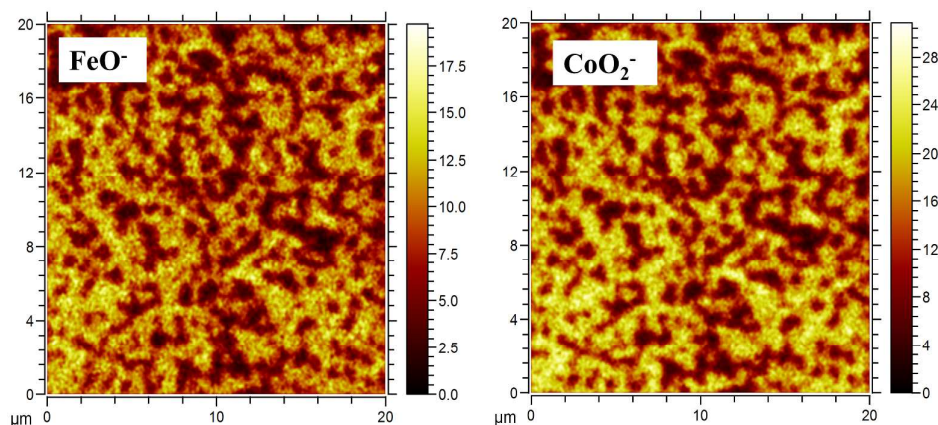


Figure 8 Secondary ion maps at $m/z = 72 \text{ u}$ ($^{56}\text{Fe}^{16}\text{O}^-$) and $m/z = 91 \text{ u}$ ($^{59}\text{Co}^{16}\text{O}_2^-$)

Discussion

The combination of ^{18}O isotopic exchange with high lateral resolution SIMS measurements shows some differences between oxygen exchange in these composites at 500 °C and at 700 °C. For both temperatures, “effective” values of D^* and k^* were obtained by fitting the diffusion profiles for the composite as if they came from a single-phase material. The effective diffusivities were higher than the values reported for single phase CGO ²⁴, which was attributed to a lower impurity content in the present material ³⁷. The k^* values were also higher than for single phase LSCF ²³, suggesting a slight enhancement in surface exchange rate for these composites.

Laterally resolved SIMS analyses of the surface isotopic fraction of the composite is more homogeneous than, for example the cation distribution. At 700 °C, the CGO actually shows a higher ^{18}O surface isotopic fraction than the LSCF, indicating that the effect is more significant than a simple diffusion of ^{18}O from the LSCF to the CGO. The apparent surface exchange coefficients for each phase (calculated from the surface isotopic fraction and literature values of D^* by means of Equation 1i) of the CGO phase increases 30 fold, whilst that of the LSCF is decreased by a factor of 0.3 - 0.4, depending on temperature. We recently reported enhancement of the surface exchange properties of CGO when treated with nitrates of the constituent cations of LSCF ⁴⁶; it is interesting to note that treatment with $\text{Sr}(\text{NO}_3)_2$ resulted in an increase in the measured k^* value by a factor of 24, a similar magnitude of enhancement to that indicated here.

In order to aid interpretation of these results, we characterised the surface composition of the composites by both ToF-SIMS and Low Energy Ion Scattering (LEIS) spectroscopy. In light of the changes in surface composition, we consider three mechanisms which may explain this, summarised in Figure 9. Briefly, these mechanisms are; 1) Catalytic spill-over, 2) Activation of the CGO surface by incorporation of transition metals and 3) cleaning of the CGO surface by the dissolution of impurities into the LSCF.

Catalytic spill-over is a process by which an active species, such as dissociated oxygen, is formed on one surface is transported to an adjacent surface which does not form that species ⁴⁷. For example, if the dissociation of oxygen is relatively fast on the LSCF surface, but incorporation there is slow, the activated oxygen may diffuse across the surface to the CGO where incorporation is relatively fast and dissociation is the rate limiting step. This has also been proposed as the active mechanism for surface exchange in YSZ-LSM composites ¹². We may also extend the spill-over mechanism to include sub-surface transfer of ^{18}O which has been incorporated on the LSCF into the

CGO. Such a mechanism may be consistent with the more homogeneous isotopic fraction seen for the composite exchanged at 500°C, but may not explain the increased surface isotopic fraction in the CGO grains of the composite exchanged at 700°C.

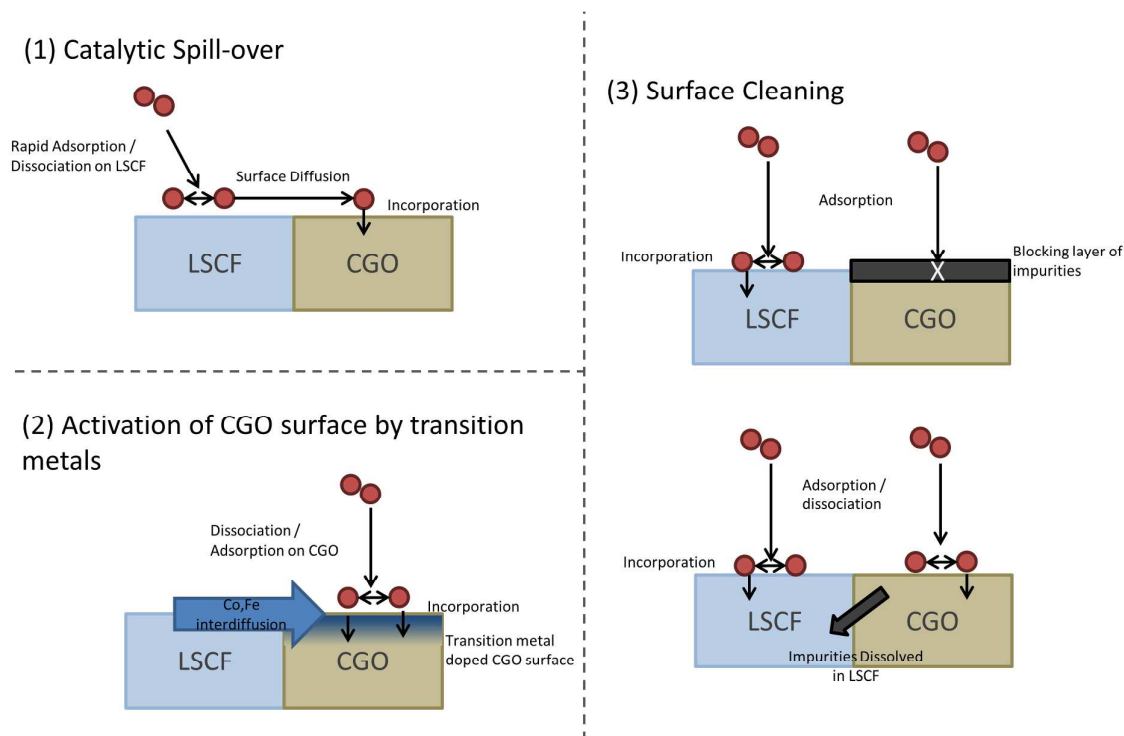


Figure 9 Schematic of possible mechanisms for surface exchange enhancement for CGO grains in composite

The second possibility to consider is that the transition metal cations could diffuse to the surfaces of the CGO, which may make the surface of the CGO catalytically active towards oxygen incorporation. In the present composites, SIMS mapping of transition metal related species (Figure 8) did not suggest any inter-diffusion of these cations into the CGO, and the concentration of transition metals at the surface measured by LEIS (Figure 6) seemed to follow the same trend as in the single phase LSCF. It is also worth noting that although in ⁴⁶, treatment of CGO surfaces with transition metal nitrates, which were subsequently decomposed to the oxides, gave a factor of 15-20 enhancement, the greatest enhancement was actually seen for the lanthanum and strontium nitrate treatments. Therefore, there does not seem to be much evidence to support this explanation for the observed enhancement.

Previous studies of the fluorite structured oxides by LEIS and ToF-SIMS indicated that there is a strong tendency for impurities such as sodium, silicon and calcium to segregate from the oxide bulk to the surface ^{42, 43, 45, 48}. Furthermore, these impurities form a layer which blocks surface

exchange⁴³, and removal of this layer leads to an increase in surface exchange coefficient. Given the solubility of the typically observed impurities (Na, Si and Ca) in the perovskite structure, and the fact that these weren't observed in the outer surface of the composite (Figure 7), we believe that the LSCF has dissolved these impurities from the CGO surface, leaving a bare "intrinsic" CGO surface, with a high surface exchange coefficient.

We note that mechanisms (1) and (3) are by no means mutually exclusive. Since the impurities can block oxygen incorporation, it is likely that a "clean" CGO surface would also be necessary for a catalytic spill-over to occur. Although further studies are warranted, *e.g.* using different grain sizes to change the surface diffusion lengths which may control these processes, we believe that mechanisms (1) and (3), or a combination of the two are more supported by the present data. We do not find any evidence to support mechanism (2), activation of the CGO surface by incorporation of transition metal cations.

Conclusions

We present results of an ¹⁸O isotope exchange-SIMS study combined with surface compositional analysis by the emerging technique of Low Energy Ion Scattering (LEIS) spectrometry. Isotope exchanges were conducted at two temperatures, 500 °C and 700 °C with subsequent analysis by ToF-SIMS, and the oxygen exchange behaviour interpreted with consideration of differences in surface composition between the single-phase end members and the composites.

It was found that for the exchange at 500 °C, the surface ¹⁸O isotope fractions at the surface of the composite were homogeneous across both phases, even though the surface isotopic fractions of single phase materials exchanged at the same time showed very different values. A feature in the ¹⁸O isotopic fraction was evident near the surface, which may be due to predominant ¹⁸O incorporation into the LSCF, some of which is subsequently transferred into the CGO phase.

At 700 °C, the ¹⁸O isotopic fraction, and apparent surface exchange coefficient, was higher for the CGO phase in the composite than for the LSCF. Several mechanisms were considered for this, in light of surface compositional analysis by LEIS and ToF-SIMS, and we believe that a combination of a catalytic spill-over and surface cleaning mechanism may be responsible for such enhancement.

Acknowledgements

The authors acknowledge support from the International Institute for Carbon Neutral Energy Research (wpi-I2CNER), funded by the World Premier Research Center Initiative of the Ministry of Education, Culture, Sports, Science and Technology. HT also acknowledges the Japanese Society for Promotion of Science for its financial support through the JSPS postdoctoral fellowship and Kakenhi Grant-in-Aid project 25-03770.

References

1. A. V. Virkar, *Int J Hydrogen Energ*, 2010, **35**, 9527-9543.
2. A. Mitterdorfer and L. J. Gauckler, *Solid State Ionics*, 1998, **111**, 185-218.
3. M. Mori, T. Abe, H. Itoh, O. Yamamoto, G. Q. Shen, Y. Takeda and N. Imanishi, *Solid State Ionics*, 1999, **123**, 113-119.
4. J. M. Ralph, C. Rossignol and R. Kumar *J. Electrochem. Soc.*, 2003, **150**, A1518-A1522.
5. E. Perry Murray, M. J. Sever and S. A. Barnett, *Solid State Ionics*, 2002, **148**, 27-34.
6. N. Sakai, H. Kishimoto, K. Yamaji, T. Horita, M. E. Brito and H. Yokokawa, *J. Electrochem. Soc.*, 2007, **154**, B1331-B1337.
7. J. D. Sirman, D. Waller and J. A. Kilner, *Cation diffusion into a CGO electrolyte*, Electrochemical Society Inc, Pennington, 1997.
8. M. Izuki, M. E. Brito, K. Yamaji, H. Kishimoto, D. H. Cho, T. Shimonosono, T. Horita and H. Yokokawa, *J Power Sources*, 2011, **196**, 7232-7236.
9. V. V. Kharton, A. V. Kovalevsky, A. P. Viskup, A. L. Shaula, F. M. Figueiredo, E. N. Naumovich and F. M. B. Marques, *Solid State Ionics*, 2003, **160**, 247-258.
10. V. V. Kharton, A. A. Yaremchenko and E. N. Naumovich, *Journal of Solid State Electrochemistry*, 1999, **3**, 303-326.
11. H. Yokokawa, N. Sakai, T. Kawada and M. Dokiya, *Solid State Ionics*, 1992, **52**, 43-56.
12. M. Dhallu, PhD, University of London, 2006.
13. M. Dhallu and J. A. Kilner, *J Fuel Cell Sci Tech*, 2005, **2**, 29-33.
14. T. Horita, K. Yamaji, N. Sakai, H. Yokokawa, T. Kato and T. Kawada, *Solid Oxide Fuel Cells Vii (Softc Vii)*, 2001, **2001**, 539-546.
15. A. K. Opitz, A. Schintlmeister, H. Hutter and J. Fleig, *Phys Chem Chem Phys*, 2010, **12**, 12734-12745.
16. J. Druce and J. A. Kilner, *In Preparation*, 2015.
17. B. Hagenhoff, *Mikrochim Acta*, 2000, **132**, 259-271.
18. R. N. S. Sodhi, *Analyst*, 2004, **129**, 483-487.

19. J. A. Kilner, S. J. Skinner and H. H. Brongersma, *Journal of Solid State Electrochemistry*, 2011, **15**, 861-876.
20. H. Tellez, A. Aguadero, J. Druce, M. Burriel, S. Fearn, T. Ishihara, D. S. McPhail and J. A. Kilner, *J Anal Atom Spectrom*, 2014, **29**, 1361-1370.
21. J. A. Kilner, H. Tellez, M. Burriel, S. Cook and J. Druce, *Solid Oxide Fuel Cells 13 (Sofc-Xiii)*, 2013, **57**, 1701-1708.
22. J. A. Kilner, B. C. H. Steele and L. Ilkov, *Solid State Ionics*, 1984, **12**, 89-97.
23. S. J. Benson, PhD, University of London, 1999.
24. P. S. Manning, J. D. Sirman and J. A. Kilner, *Solid State Ionics*, 1996, **93**, 125-132.
25. H. Tellez, J. Druce, J. E. Hong, T. Ishihara and J. A. Kilner, 2015.
26. J. Crank, *The Mathematics of Diffusion*, Clarendon (Oxford University Press), Oxford, UK, 1979.
27. R. A. De Souza, J. Zehnpfenning, M. Martin and J. Maier, *Solid State Ionics*, 2005, **176**, 1465-1471.
28. H. H. Brongersma, M. Draxler, M. de Ridder and P. Bauer, *Surf Sci Rep*, 2007, **62**, 63-109.
29. H. H. Brongersma, in *Characterization of Materials*, John Wiley & Sons, Inc., 2012.
30. H. H. Brongersma, T. Grehl, P. A. van Hal, N. C. W. Kuijpers, S. G. J. Mathijssen, E. R. Schofield, R. A. P. Smith and H. R. J. ter Veen, *Vacuum*, 2010, **84**, 1005-1007.
31. M. de Ridder, R. G. van Welzenis and H. H. Brongersma, *Surf Interface Anal*, 2002, **33**, 309-317.
32. E. Jud, Z. Zhang, W. Sigle and L. Gauckler, *J Electroceram*, 2006, **16**, 191-197.
33. S. Taub, R. E. A. Williams, X. Wang, D. W. McComb, J. A. Kilner and A. Atkinson, *Acta Materialia*, 2014, **81**, 128-140.
34. R. A. De Souza, J. A. Kilner and J. F. Walker, *Materials Letters*, 2000, **43**, 43-52.
35. Y. C. Chung and B. J. Wuensch, *J Appl Phys*, 1996, **79**, 8323-8329.
36. A. Esquirol, J. Kilner and N. Brandon, *Solid State Ionics*, 2004, **175**, 63-67.
37. J. Druce, PhD, University of London, 2010.
38. R. J. Chater, S. Carter, J. A. Kilner and B. C. H. Steele, *Solid State Ionics*, 1992, **53**, 859-867.
39. D. McPhail and M. Dowsett, in *Surface Analysis - The Principal Techniques*, John Wiley & Sons, Ltd, 2009, pp. 207-268.
40. G. Holzlechner, M. Kubicek, H. Hutter and J. Fleig, *J Anal Atom Spectrom*, 2013, **28**, 1080-1089.

41. J. Druce, H. Tellez, M. Burriel, M. D. Sharp, L. J. Fawcett, S. N. Cook, D. S. McPhail, T. Ishihara, H. H. Brongersma and J. A. Kilner, *Energ Environ Sci*, 2014, **7**, 3593-3599.
42. P. J. Scanlon, R. A. M. Bink, F. P. F. van Berkel, G. M. Christie, L. J. van Ijzendoorn, H. H. Brongersma and R. G. Van Welzenis, *Solid State Ionics*, 1998, **112**, 123-130.
43. M. de Ridder, A. G. J. Vervoort, R. G. van Welzenis and H. H. Brongersma, *Solid State Ionics*, 2003, **156**, 255-262.
44. J. Druce, T. Ishihara and J. Kilner, *Solid State Ionics*, 2014, **262**, 893-896.
45. M. de Ridder, R. G. van Welzenis, H. H. Brongersma, S. Wulff, W. F. Chu and W. Weppner, *Nucl Instrum Meth B*, 2002, **190**, 732-735.
46. J. Druce and J. A. Kilner, *J. Electrochem. Soc.*, 2014, **161**, F99-F104.
47. W. C. Conner and J. L. Falconer, *Chem Rev*, 1995, **95**, 759-788.
48. K. V. Hansen, K. Norrman and M. Mogensen, *Surf Interface Anal*, 2006, **38**, 911-916.